

 Open access • Journal Article • DOI:10.1038/NMETH.4605

## Quantitative mapping and minimization of super-resolution optical imaging artifacts

— [Source link](#) 

Siân Culley, David Albrecht, Caron Jacobs, Pedro M. Pereira ...+5 more authors

**Institutions:** University College London, Francis Crick Institute, Aix-Marseille University

**Published on:** 19 Feb 2018 - Nature Methods (Nature Publishing Group)

**Topics:** Image quality

Related papers:

- [Imaging intracellular fluorescent proteins at nanometer resolution.](#)
- [Sub-diffraction-limit imaging by stochastic optical reconstruction microscopy \(STORM\).](#)
- [Fast live-cell conventional fluorophore nanoscopy with ImageJ through super-resolution radial fluctuations.](#)
- [ThunderSTORM: a comprehensive ImageJ plug-in for PALM and STORM data analysis and super-resolution imaging](#)
- [Measuring image resolution in optical nanoscopy.](#)

Share this paper:    

View more about this paper here: <https://typeset.io/papers/quantitative-mapping-and-minimization-of-super-resolution-47xwfuf2v0>



**HAL**  
open science

## Quantitative mapping and minimization of super-resolution optical imaging artifacts

Siân Culley, David Albrecht, Caron Jacobs, Pedro Matos Pereira, Christophe Leterrier, Jason Mercer, Ricardo Henriques

► **To cite this version:**

Siân Culley, David Albrecht, Caron Jacobs, Pedro Matos Pereira, Christophe Leterrier, et al.. Quantitative mapping and minimization of super-resolution optical imaging artifacts. *Nature Methods*, Nature Publishing Group, 2018, 15 (4), pp.263-266. 10.1038/nmeth.4605 . hal-01736919

**HAL Id: hal-01736919**



**<https://hal.archives-ouvertes.fr/hal-01736919>**

Submitted on 20 Apr 2018

**HAL** is a multi-disciplinary open access archive for the deposit and dissemination of scientific research documents, whether they are published or not. The documents may come from teaching and research institutions in France or abroad, or from public or private research centers.

L'archive ouverte pluridisciplinaire **HAL**, est destinée au dépôt et à la diffusion de documents scientifiques de niveau recherche, publiés ou non, émanant des établissements d'enseignement et de recherche français ou étrangers, des laboratoires publics ou privés.

# Quantitative mapping and minimization of super-resolution optical imaging artifacts

Siân Culley<sup>1-3</sup>, David Albrecht<sup>1</sup>, Caron Jacobs<sup>1,2</sup>, Pedro Matos Pereira<sup>1-3</sup> , Christophe Leterrier<sup>4</sup> , Jason Mercer<sup>1</sup> & Ricardo Henriques<sup>1-3</sup> 

**Super-resolution microscopy depends on steps that can contribute to the formation of image artifacts, leading to misinterpretation of biological information. We present NanoJ-SQUIRREL, an ImageJ-based analytical approach that provides quantitative assessment of super-resolution image quality. By comparing diffraction-limited images and super-resolution equivalents of the same acquisition volume, this approach generates a quantitative map of super-resolution defects and can guide researchers in optimizing imaging parameters.**

The quality and resolution of super-resolution images is dependent on several factors, including the photophysics of fluorophores used, the chemical environment of the sample, the imaging conditions, and the analytical approaches used to produce final images<sup>1-5</sup> (**Supplementary Note 1**). Thus far, super-resolution data quality assessment has relied on subjective comparison of the data relative to prior knowledge of the expected structures<sup>6,7</sup> or benchmarking of the data against other high-resolution imaging methods such as electron microscopy<sup>8</sup>. An exception exists in the field of structured illumination microscopy (SIM)<sup>9</sup>, where analytical frameworks exist for quantitative evaluation of image quality<sup>10,11</sup>.

The simplest way to visually identify defects in super-resolution images is the direct comparison of diffraction-limited and super-resolved images of the sample. For images that represent the same focal volume, the super-resolution version should provide an improved resolution representation of the reference diffraction-limited image. When this analysis is performed empirically, it is subject to human bias and interpretation. Here we present an analytical approach that allows the quantitative mapping of local image errors, providing a framework to assist in reducing these errors. We name this approach SQUIRREL (super-resolution quantitative image rating and reporting of error locations); it is

implemented as an open-source ImageJ and Fiji<sup>12</sup> plugin (NanoJ-SQUIRREL), exploiting high-performance graphics processing unit (GPU)-enabled computing.

SQUIRREL is based on the premise that a super-resolution image should be a high-precision representation of the underlying nanoscale positions and photon emission of the imaged fluorophores. The algorithm requires three inputs: a reference image (generally diffraction limited), a super-resolution image, and a representative resolution scaling function (RSF) image. The RSF can be provided by the user or automatically estimated through optimization (**Supplementary Note 2**). Assuming an imaged field of view has a spatially invariant point-spread function (PSF), application of the RSF to the super-resolution image should produce an image with a high degree of similarity to the original diffraction-limited one. Variance between these images beyond a noise floor can be used as a quantitative indicator of local macro-anomalies in the super-resolution representation (**Fig. 1** and **Supplementary Note 1**). Although this approach is based on the principle of comparing conventional and super-resolution images, in contrast to other approaches it requires no prior knowledge of the expected properties of the sample or label.

The stages involved in error mapping are (1) correcting for any analytical or optical spatial offsets between the super-resolution and reference images; (2) iterative estimation of the RSF and linear rescaling coefficients to convert the super-resolution image into its diffraction-limited equivalent (the ‘resolution-scaled image’); (3) calculation of the pixel-wise absolute difference between the reference and resolution-scaled image to generate the final error map (**Fig. 1a**). In addition to local quality assessment, we calculate two global image quality metrics: the resolution-scaled error (RSE), representing the root-mean-square error between the reference and resolution-scaled image; and the RSP (resolution-scaled Pearson coefficient), which is the Pearson correlation coefficient between the reference and resolution-scaled images with values truncated between  $-1$  and  $1$ . The RSE is more sensitive to differences in contrast and brightness; the RSP provides a score of image quality that can be compared across different super-resolution imaging modalities. A full description of the SQUIRREL algorithm is provided in **Supplementary Note 3**.

To demonstrate the capacity of SQUIRREL to identify defects in super-resolution images, we acquired total internal reflectance fluorescence (TIRF) microscopy images of immunolabeled microtubules (**Fig. 1b**) and a corresponding dSTORM<sup>4</sup> data set. From these we produced an error map indicating regions of high dissimilarity (**Fig. 1c**). As might be expected, regions surrounding filament junctions and overlapping filaments, where the increased local density of fluorophores limits the capacity

<sup>1</sup>MRC-Laboratory for Molecular Cell Biology, University College London, London, UK. <sup>2</sup>Department of Cell and Developmental Biology, University College London, London, UK. <sup>3</sup>The Francis Crick Institute, London, UK. <sup>4</sup>Aix Marseille Université, CNRS, INP UMR7051, Marseille, France. Correspondence should be addressed to C.L. (christophe.leterrier@univ-amu.fr), J.M. (jason.mercer@ucl.ac.uk) or R.H. (r.henriques@ucl.ac.uk).

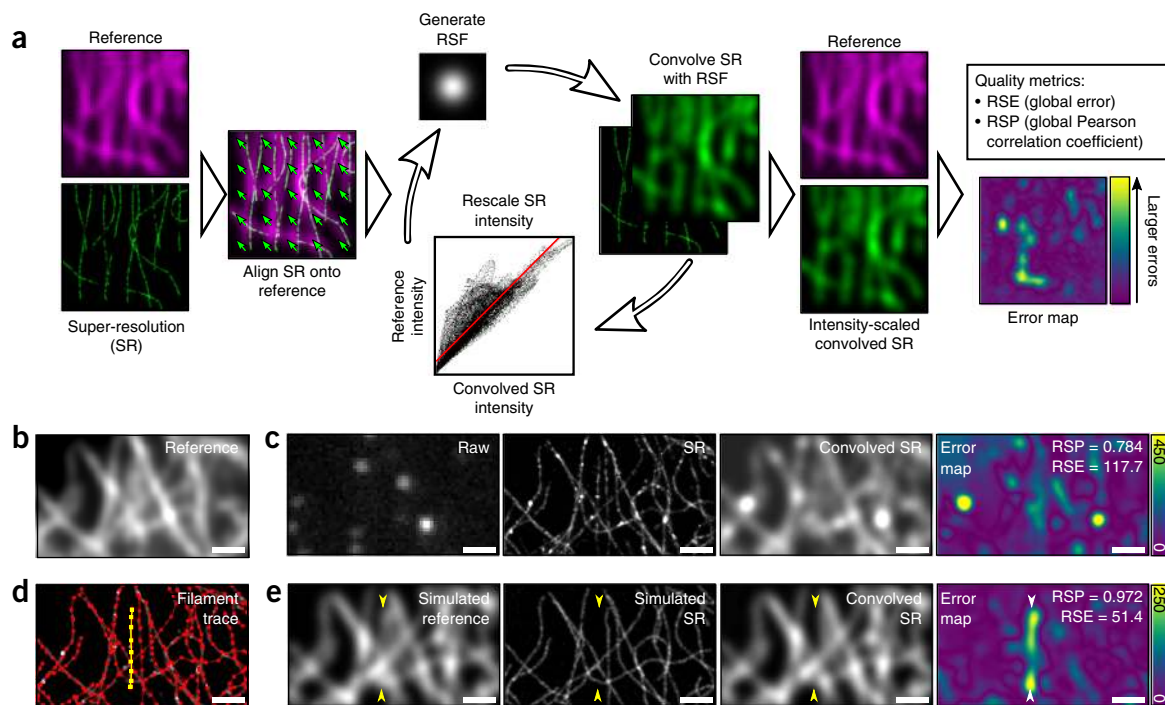


**Figure 1** | Overview of quantitative error mapping with SQUIRREL. **(a)** Representative workflow for SQUIRREL error mapping. **(b)** Fixed microtubules labeled with Alexa Fluor 647 imaged in TIRF. **(c)** Panels show: a single frame from raw dSTORM acquisition of structure in **(b)** ('Raw'), super-resolution reconstruction of dSTORM data set ('SR'), super-resolution image convolved with appropriate RSF ('Convolved SR'), and quantitative map of errors between reference and convolved SR images ('Error map'; color bar indicates magnitude of the error). **(d)** SuReSim<sup>13</sup> filament tracing used to simulate images in **(e)**; yellow filament is present in reference image but absent in super-resolution image. **(e)** Simulated reference image, super-resolution image, super-resolution image convolved with RSF, and error map. Yellow arrowheads indicate position of yellow filament seen in **(d)**. Scale bars in **(b-e)**, 1  $\mu\text{m}$ . **(b-d)** represents data from one of five independent experiments showing similar results.

for single-molecule localizations, were particularly dissimilar. We further used these images to simulate two optically and photophysically realistic data sets using the SuReSim software<sup>13</sup> (Fig. 1d,e): a diffraction-limited reference data set containing all the traced filaments and an artifactual dSTORM data set in which a filament was removed. SQUIRREL analysis of the simulated reference and artifactual super-resolution image produced an error map that clearly highlights the absence of the selected filament (Fig. 1e). These results exemplify the power of SQUIRREL to identify large-scale image artifacts in instances in which subjective comparison of the widefield and super-resolution images would be insufficient.

SQUIRREL is not sensitive only to the disappearance of structures. It can also identify common super-resolution artifacts, including merged structures and bright aggregates (Supplementary Note 1). The software is not limited to single-molecule localization microscopy (SMLM); for SIM images, it provides complementary information to SIMcheck<sup>10</sup> (Supplementary Note 4).

Out-of-focus information affects SQUIRREL metrics (Supplementary Note 5), so that SQUIRREL cannot highlight errors in the axial direction. For example, using widefield references of thick samples compromises RSP and RSE fidelity, although this can be minimized by using optical-sectioning systems such as TIRF (Supplementary Note 5), confocal, and lattice light-sheet microscopes. Through simulation and analysis of 3D structures incorporating defects (Supplementary Note 5), we estimate that SQUIRREL is capable of accurately identifying 2D image artifacts within an  $\sim 600\text{-nm}$  focal depth.

The major limitation of SQUIRREL is that small-scale artifacts cannot be identified, owing to the diffraction-limited reference image. To define this limit we carried out simulations of an eight-molecule ring structure of varying diameter; for signal-to-noise ratios typically encountered in super-resolution microscopy, SQUIRREL can quantify image anomalies as small as 150 nm (Supplementary Note 6). This limit is set by the resolution of the reference image. Using a higher-resolution image (for instance, acquired using another super-resolution modality) as the reference can provide smaller-scale artifact detection and cross-validation. To demonstrate this, we performed correlative SMLM, SIM, super-resolution radial fluctuations (SRRF)<sup>14</sup>, and stimulated emission depletion (STED) microscopy on vaccinia virus (VACV) lateral bodies<sup>15</sup>, structures separated by  $<200\text{ nm}$ . Using SQUIRREL to cross-validate different super-resolution techniques, we found that artifacts not discernible using a diffraction-limited reference image were highlighted (Supplementary Note 7).

Image resolution is commonly used as a reporter of image quality, although in super-resolution studies these factors correlate weakly<sup>6,7,16</sup>. One popular method for quantifying image resolution in super-resolution and electron microscopy is Fourier ring correlation (FRC)<sup>16</sup>, which conventionally represents the global resolution of an image. Within the NanoJ-SQUIRREL package, we have implemented block-wise FRC resolution mapping to provide local resolution measurements (Supplementary Note 8). We mapped the local FRC-estimated resolution of a dSTORM data set and compare it against the SQUIRREL error map. Highlighting various regions of the data set (Fig. 2a,b), we observe that

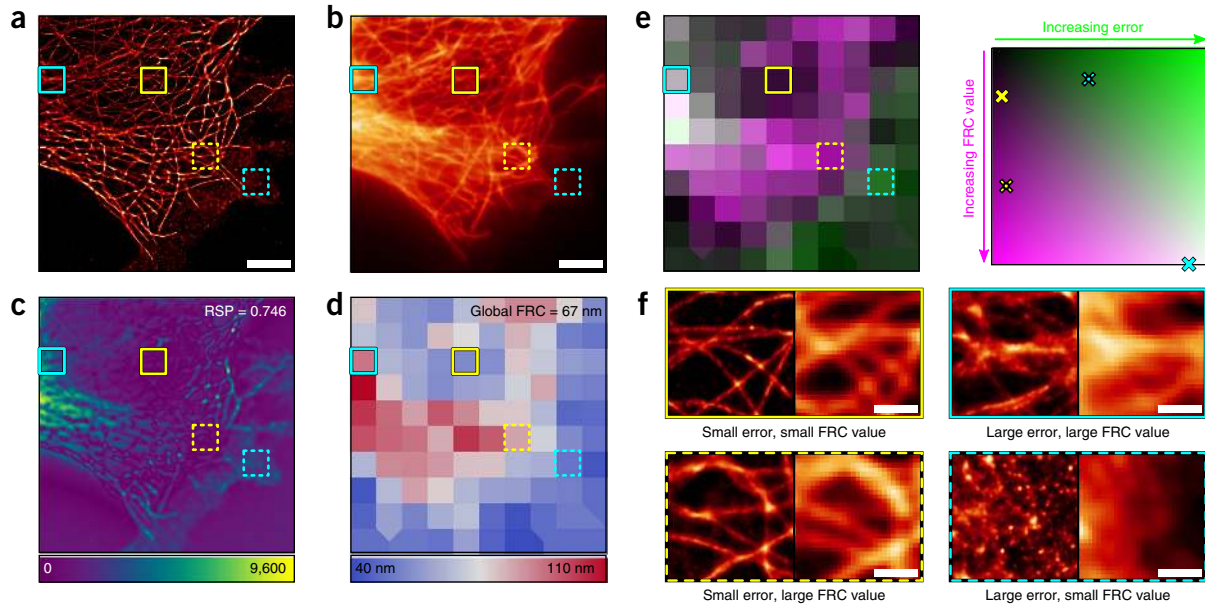


**Figure 2** | Error mapping and FRC analysis. (a) Super-resolution image of fixed Alexa Fluor 647-labeled microtubules reconstructed via MLE. (b) Corresponding TIRF image. (c) Error map for super-resolution image in **a** using **b** as the reference. (d) Local mapping of FRC values for super-resolution image in **a**. (e) Left, merge of FRC map (magenta) and error map (green, binned to match FRC map). Right, corresponding color map of error-resolution space for this image; crosses indicate colors used for boxed regions. (f) Enlargements of super-resolution (left) and widefield (right) boxed regions in **a–e**. Scale bars in **a,b**, 5  $\mu\text{m}$ ; in **f**, 1  $\mu\text{m}$ . Figure represents data from one of five independent experiments showing similar results.

high resolution does not necessarily correlate with low error (Fig. 2c–f). Thus SQUIRREL error mapping allows direct visual detection of structural anomalies in a super-resolution image without coupling quality to a description of resolution.

By providing an assessment of image quality, SQUIRREL can be used as a tool to improve various aspects of super-resolution image acquisition. One of these is the choice of analytical method for SMLM image reconstruction. As dozens of

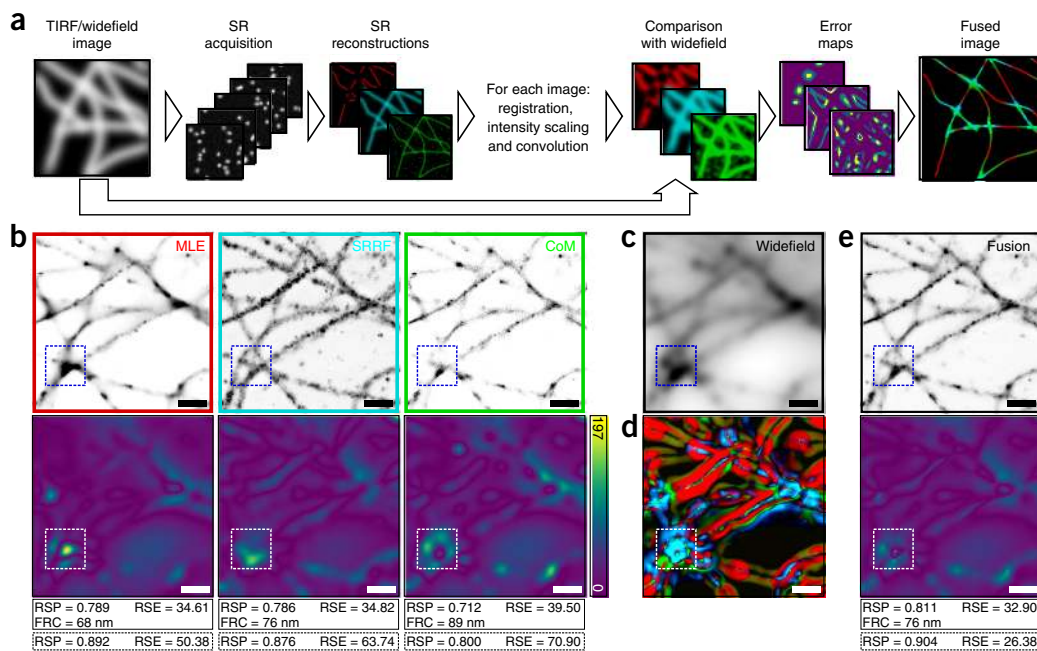


**Figure 3** | Image fusion of SMLM data using SQUIRREL. (a) Workflow for fusing different super-resolution images constructed from the same SMLM data set. (b) Top row, super-resolution images generated from the same dSTORM data set using the indicated algorithms: MLE, maximum likelihood estimator with multiemitter fitting; SRRF, super-resolution radial fluctuations; CoM, center of mass. Bottom row, corresponding error maps with the widefield image in **c** used as reference. (d) Contributions of different images to the final fused images, color coded as **b** top. (e) Top, fused image; bottom, error map of fused image, with **c** again used as reference image. Values in solid line boxes indicate the quality metrics of the whole images; values in dashed boxes represent quality values from highlighted inset region only. Scale bars, 1  $\mu\text{m}$ . **b–e** represent data from one of five independent experiments showing similar results.

high-performing algorithms are available<sup>5</sup>, it can be challenging to determine which will be most appropriate for a given data set. We acquired a dSTORM data set of immunolabeled microtubules and analyzed it using three distinct algorithms: ThunderSTORM using a multiemitter maximum likelihood estimator engine<sup>17</sup>, SRRF, and QuickPALM<sup>18</sup>. SQUIRREL error maps and quality metrics were generated for these three super-resolution images (Fig. 3a,b) using the same diffraction-limited reference image for each (Fig. 3c). In addition to providing the means to ‘rank’ the quality of each reconstruction, the error maps provide spatial details on the local accuracy of each algorithm. By converting these into weights (Fig. 3d and Supplementary Note 9), a new composite image with minimal defects can be generated using the lowest-error features of each reconstruction (Fig. 3e). SQUIRREL can also be used to empirically optimize super-resolution images, as exemplified by determination of the optimal DNA-PAINT imaging conditions for clathrin-coated pits (Supplementary Note 10) and the optimal number of frames for dSTORM imaging of neuronal actin rings along axons (Supplementary Note 11).

In conclusion, SQUIRREL is a quick and easy approach to improve super-resolution data acquisition and quality. We envisage that this approach will eventually be implemented for continual monitoring of super-resolution image quality during acquisition. By pairing such a feedback approach with automated adaptation of acquisition parameters, users could ensure optimal image quality, shorten acquisition times, and reduce data storage requirements.

## METHODS

Methods, including statements of data availability and any associated accession codes and references, are available in the [online version of the paper](#).

*Note: Any Supplementary Information and Source Data files are available in the online version of the paper.*

## ACKNOWLEDGMENTS

We thank A. Knight (Holistx Ltd.) and S. Holden (Newcastle University) for critical reading of the manuscript; J. Ries (European Laboratory for Molecular Biology, Heidelberg) for provision of customized MATLAB software and critical reading of the manuscript; K. Tosheva (University College London) for critical reading of the manuscript and beta testing of the software; and B. Baum (University College London) for reagents. Many of the look-up tables used here are based on the open-source repository of D. Williamson at King’s

College London. This work was funded by grants from the UK Biotechnology and Biological Sciences Research Council (BB/M022374/1; BB/P027431/1; BB/R000697/1) (R.H. and P.M.P.), MRC Programme Grant (MC\_UU12018/7) (J.M.), the European Research Council (649101–UbiProPox) (J.M.), the UK Medical Research Council (MR/K015826/1) (R.H. and J.M.), the Wellcome Trust (203276/Z/16/Z) (S.C. and R.H.) and the Centre National de la Recherche Scientifique (CNRS ATIP-AVENIR program A02016) (C.L.). D.A. is presently a Marie Curie fellow (Marie Skłodowska-Curie grant agreement No 750673). C.J. funded by a Commonwealth scholarship, funded by the UK government.

## AUTHOR CONTRIBUTIONS

S.C. and R.H. devised the conceptual framework and derived theoretical results. S.C., D.A., C.L., J.M., and R.H. planned experiments. S.C. and R.H. wrote the algorithm. Simulations were done by S.C. Experimental data sets were acquired by S.C. (Fig. 1), D.A. (Fig. 2; Supplementary Notes 4 and 7), C.J. (Fig. 2 and Supplementary Note 9), P.M.P. (Fig. 3), and C.L. (Supplementary Notes 5, 10, and 11). Data were analyzed by S.C. and D.A.; and C.L., J.M., and R.H. provided research advice. The paper was written by S.C., D.A., J.M., and R.H. with editing contributions from all the authors.

## COMPETING FINANCIAL INTERESTS

The authors declare no competing financial interests.

Reprints and permissions information is available online at <http://www.nature.com/reprints/index.html>. Publisher’s note: Springer Nature remains neutral with regard to jurisdictional claims in published maps and institutional affiliations.

- Dempsey, G.T., Vaughan, J.C., Chen, K.H., Bates, M. & Zhuang, X. *Nat. Methods* **8**, 1027–1036 (2011).
- Almada, P., Culley, S. & Henriques, R. *Methods* **88**, 109–121 (2015).
- Pereira, P.M., Almada, P. & Henriques, R. *Methods Cell Biol.* **125**, 95–117 (2015).
- van de Linde, S. *et al. Nat. Protoc.* **6**, 991–1009 (2011).
- Sage, D. *et al. Nat. Methods* **12**, 717–724 (2015).
- Pengo, T., Olivier, N. & Manley, S. Preprint at <https://arxiv.org/abs/1501.05807> (2015).
- Fox-Roberts, P. *et al. Nat. Commun.* **8**, 13558 (2017).
- Betzig, E. *et al. Science* **313**, 1642–1645 (2006).
- Gustafsson, M.G. *J. Microsc.* **198**, 82–87 (2000).
- Ball, G. *et al. Sci. Rep.* **5**, 15915 (2015).
- Förster, R., Wicker, K., Müller, W., Jost, A. & Heintzmann, R. *Opt. Express* **24**, 22121–22134 (2016).
- Schindelin, J. *et al. Nat. Methods* **9**, 676–682 (2012).
- Venkataramani, V., Herrmannsdörfer, F., Heilemann, M. & Kuner, T. *Nat. Methods* **13**, 319–321 (2016).
- Gustafsson, N. *et al. Nat. Commun.* **7**, 12471 (2016).
- Cyrklaff, M. *et al. Proc. Natl. Acad. Sci. USA* **102**, 2772–2777 (2005).
- Nieuwenhuizen, R.P.J. *et al. Nat. Methods* **10**, 557–562 (2013).
- Ovesný, M., Křížek, P., Borkovec, J., Švindrych, Z. & Hagen, G.M. *Bioinformatics* **30**, 2389–2390 (2014).
- Henriques, R. *et al. Nat. Methods* **7**, 339–340 (2010).

## ONLINE METHODS

**Super-resolution image simulation with SuReSim.** In order to simulate disappearance of a filament from a realistic microtubule network, a real super-resolution image of microtubules (**Fig. 1c**) was used as a support for SuReSim data simulation. Raw data of blinking Alexa 647-labeled microtubules imaged using TIRF were reconstructed using ThunderSTORM maximum likelihood multiemitter fitting and then loaded into the SuReSim software and all filaments were traced using the editor function and the WIMP file saved. SuReSim was used to generate a simulated super-resolution reconstruction of all filaments, which was then convolved by a Gaussian PSF to generate a simulated reference image. The object in the WIMP file corresponding to the filament highlighted in **Figure 1d,e** was deleted, and SuReSim was used again to render a simulated super-resolution reconstruction, except this time missing a filament. SuReSim was also used for the simulations in **Supplementary Note 1**.

**Cell lines and primary cells.** HeLa cells (**Figs. 1 and 2**) were kindly provided by M. Marsh, MRC LMCB, University College London, and cultured in phenol red-free DMEM (Gibco) supplemented with 2 mM GlutaMAX (Gibco), 50 U/ml penicillin, 50 µg/ml streptomycin and 10% FBS (FBS; Gibco). CHO cells (**Fig. 3**) were cultured in phenol red-free Minimum Essential Medium Alpha (MEM $\alpha$ ; Gibco) supplemented with 10% FBS (Gibco) and 1% penicillin/streptomycin (Sigma).

Rat hippocampal neurons and glial cells (**Supplementary Notes 10 and 11**) were harvested from embryonic day 18 pups, following established guidelines of the European Animal Care and Use Committee (86/609/CEE) and approval of the local ethics committee (agreement D13-055-8), and cultured in Neurobasal medium (Gibco) supplemented with 2 mM GlutaMAX-I (Gibco) and B27 supplement (Gibco). All cells were grown at 37 °C in a 5% CO<sub>2</sub> humidified incubator.

**Sample preparation for fixed microtubules.** For TIRF-SMLM imaging of microtubules (**Figs. 1 and 2**), 13 mm diameter, thickness #1.5 coverslips were washed overnight in 1:1 HCl:methanol and washed 5 times in ddH<sub>2</sub>O and twice in 90% isopropyl alcohol. Coverslips were then incubated overnight in poly-L-lysine (0.01%) (Sigma Aldrich) and rinsed twice in PBS. HeLa cells were seeded on these coverslips and grown overnight in 12-well plates. Cells were fixed with 4% PFA in cytoskeleton buffer (10 mM MES, pH 6.1, 150 mM NaCl, 5 mM EGTA, 5 mM glucose, 5 mM MgCl<sub>2</sub>) for 15 min at 37 °C, washed 3× with PBS, then permeabilized with 0.1% Triton X-100 in PBS for 10 min and blocked in 2.5% BSA in PBS for a further 30 min. Samples were then labeled with 2 µg/ml anti- $\alpha$ -tubulin (DM1A mouse monoclonal, Sigma Aldrich) in 2.5% BSA in PBS for 1 h, followed by 3× washes with PBS and labeling with Alexa Fluor 647-labeled goat anti-mouse secondary antibody (Invitrogen) (2 µg/ml in 2.5% BSA in PBS) for 1 h. Samples were washed 3× with PBS and fixed again in 4% PFA in cytoskeleton buffer for 10 min, before being washed 3× with PBS. Samples were mounted on a Parafilm-formed gasket<sup>3</sup> in STORM buffer (150 mM Tris, pH 8, 10 mM NaCl, 1% glycerol, 1% glucose, 1% BME), sealed with clear nail varnish (Maybelline) and imaged within 3 h of mounting.

For imaging in different focal volumes (**Supplementary Note 5**), COS cells were fixed with glutaraldehyde and labeled

with two monoclonal mouse anti- $\alpha$ -tubulin antibodies (DM1A and B-5-1-2, both from Sigma) and a goat anti-mouse Alexa Fluor 647-labeled secondary antibody (Thermo Fisher Scientific). Samples were mounted in Smart Buffer (Abbelight) for imaging.

For widefield super-resolution imaging of microtubules (**Fig. 3**), CHO cells were seeded on ultra-clean<sup>3</sup> 8 mm diameter thickness #1.5 coverslips (Zeiss) at a density of  $1 \times 10^5$  per 35 mm dish. Fixation was performed with 4% PFA in a modified version of cytoskeleton stabilizing buffer (CSB) (5 mM KCl, 0.1 mM NaCl, 4 mM NaHCO<sub>3</sub>, 11 mM Na<sub>2</sub>HPO<sub>4</sub>, 2 mM MgCl<sub>2</sub>, 5 mM PIPES, 2 mM EGTA, pH 6.9) for 15 min at 37 °C, followed by washing with the same CSB (without PFA). Additional permeabilization was performed (0.05% Triton X-100 in CSB) for 5 min followed by three washing steps using 0.05% Tween-20 in the modified version of CSB and blocking in 5% BSA (Sigma) for 40 min. Microtubules were stained and submitted to a secondary fixation step as described above. 100 nm TetraSpeck beads (Life Technologies) were added at a dilution of 1:1000 in PBS for 10 min to each coverslip. Coverslips were mounted on clean microscope slides<sup>3</sup> in 100 mM mercaptoethylamine (Sigma) at pH 7.3 and all imaging was performed within 3 h of mounting.

**Fixed microtubule imaging.** Fixed microtubule samples were imaged by TIRF-SMLM (**Figs. 1 and 2**) on a N-STORM microscope (Nikon Instruments), using a 100× TIRF objective (Plan-APOCHROMAT 100×/1.49 Oil, Nikon) with additional 1.5× magnification. A reference TIRF image was acquired with 5% power 647 nm laser illumination and 100 ms exposure time, before SMLM data acquisition of 40 000 frames at 100% power 647 nm illumination with 405 nm stimulation and an exposure time of 30 ms per frame.

Imaging with different illumination regimes (**Supplementary Note 5**) was performed on an N-STORM microscope using a 100×, 1.49 NA objective as above, but with no additional magnification and an exposure time of 15 ms. Prior to dSTORM imaging a reference image was acquired using a high-pressure mercury lamp (Intensilight, Nikon) with a Cy5 filter cube (Nikon); the filter cube was then switched and the laser illumination set to either vertical (i.e. widefield), HILO, or TIRF. A second reference image was then acquired, this time with laser illumination. A cylindrical lens was inserted into the detection path and 60,000 frame dSTORM data set acquired at this angle.

Widefield and super-resolution imaging for fusion (**Fig. 3**) was carried out on a Zeiss Elyra PS.1 inverted microscope system, using a 100× TIRF objective (PlanAPOCHROMAT 100×/1.46 Oil, Zeiss) and additional 1.6× magnification. The sample was illuminated with a 642 nm laser operating at 100% laser power. 45000 frames were acquired with a 20 ms exposure time per frame.

**Reconstruction algorithms for dSTORM data.** The freely available software packages ThunderSTORM<sup>17</sup> (**Figs. 1–3**, **Supplementary Notes 5, 7, and 10**), SRRF (**Fig. 3**; **Supplementary Notes 7 and 10**) and QuickPALM<sup>18</sup> (**Fig. 3** and **Supplementary Note 10**) were used for super-resolution image reconstruction. Images labeled ‘MLE’ were reconstructed with ThunderSTORM with the integrated PSF method with maximum likelihood fitting and multiemitter fitting enabled. Drift correction was performed post-localization and images were rendered using a normalized 20 nm Gaussian. Images labeled ‘SRRF’ were analyzed

with the most appropriate parameters for each individual data set and drift corrected during analysis. Images labeled 'CoM' were reconstructed using QuickPALM with the default parameters, following drift correction of the raw data using the NanoJ-SRRF package. The particle tables from QuickPALM were then loaded into ThunderSTORM for rendering using a normalized 20 nm Gaussian.

**SIM imaging.** For SQUIRREL analysis of SIM images (Supplementary Note 4), FluoCells prepared slide #2 (Invitrogen) with BPAE cells stained with Texas Red-X phalloidin and Alexa Fluor 488-tubulin was imaged on a Zeiss Elyra PS.1 system, using a 63× NA 1.4 objective with additional 1.6× magnification for SIM and widefield acquisition. For actin imaging, 'Low SNR' images were acquired with a 561 nm laser at 0.05% laser power, using 100 ms exposure time, and 5 grid rotations. 'High SNR' images were acquired with a 561 nm laser at 5% laser power, 100 ms exposure, 5 grid rotations. Widefield images were acquired with a 561 nm laser at 0.2% laser power, 100 ms exposure time. SIM reconstructions were generated with the Zeiss Elyra Zen software using automatic settings. For microtubule imaging, raw SIM data were acquired with a 488 nm laser at 10% laser power using 100 ms exposure time and three grid rotations. The SIM reconstruction was generated using FairSIM<sup>19</sup>.

**Generation and analysis of synthetic data at different z-positions.** The bead images used in Supplementary Note 5 were obtained from the open source data set 'z-stack-Bead-2D-Exp-as-stack' available to download from the SMLMS Challenge 2016 website,

<http://bigwww.epfl.ch/smlm/challenge2016/datasets/Beads/Data/data.html> (data used here were downloaded on 4th September 2017). This data set comprises 151 slices of an image of six fluorescent beads covering the z-range -750 nm to 750 nm (step size = 10 nm). The central x,y location of each of the six beads in this was determined at the central plane of the z-stack, and this was used to define the center of a 3.3 μm × 3.3 μm region about each bead. For generation of the data set containing PSFs from all z-positions in each frame, these regions were pasted into an image where the x,y coordinates mapped to a specific z-position from the bead image stack. The target x,y coordinates for pasting the images were spaced such that there was 5 μm between adjacent bead centers, and regions were randomly from the six original bead images. This was repeated 1000 times to generate a 1000-frame data set. Gaussian-Poisson noise was then added to the image stack to mask the edges of the pasted bead images. This data set was then analyzed with SRRF and ThunderSTORM (default software settings in both cases) to produce a single super-resolution image for each algorithm. The reference image was an average projection of all 1000 frames. For generation of the data set containing constant z-positions in each frame, regions from the bead z-stack were again selected and pasted but this time z was varied between slices as opposed to the x,y position within each frame. 10 frames were produced for each z-position, and noise was added again as above. ThunderSTORM and SRRF analyses (default settings) were then run on this image stack 10 slices at a time to generate a single super-resolution image for each z-position. The reference was the average of the 10 frames corresponding to z = 0 nm.

For assessing the impact of out-of-focus fluorescence on defect detection (Supplementary Note 5), a test structure was simulated consisting of three semicircles of radius 500 nm and axial tilt ranging from -50 nm to +750 nm. A widefield representation of this structures was produced via convolution with a 3D PSF generated using the ImageJ PSF Generator plugin<sup>20</sup> with the following settings: Born and Wolf optical model, numerical aperture 1.4, wavelength 640 nm, z-range 1500 nm, z-step size 2 nm. Single molecule blinking data sets were generated with custom-written simulation software with the same PSF used for rendering molecule appearances, and were binned into 100 nm 'camera' pixels with Gaussian-Poisson noise. This was performed for both the defect-free structure and an artifactual equivalent where 100 nm stretches of the structure had been deleted. These data sets were analyzed using weighted-least-squares fitting in ThunderSTORM.

**VACV sample preparation and imaging.** 2.5 × 10<sup>6</sup> VACV particles (WR strain, EGFP-F18 in *tk* locus<sup>21</sup>) were diluted in 100 μl 1 mM TRIS, pH 8, sonicated for 3 × 30 s and incubated on grid-<sup>ed</sup> #1.5 glass-bottom petri dishes (Zell-Kontakt GmbH) for 1 h at room temperature and fixed with 4% PFA in PBS for 15 min. Samples were quenched with 50 mM NH<sub>4</sub>Cl in PBS for 10 min, washed in PBS, and incubated in permeabilization/blocking buffer (1% Triton X-100, 5% BSA, 1% FBS in PBS) for 30 min. Samples were labeled in blocking/permeabilization buffer overnight at 4 °C or 2 h at room temperature with anti-GFP nanobodies (Chromotek), labeled in-house with Alexa Fluor 647 NHS-ester (Life Technologies) with a dye-to-protein ratio of approximately 1, as previously described<sup>22</sup>. Samples were then washed 3× with PBS, fixed in 4% PFA in PBS for 10 min, quenched with 50 mM NH<sub>4</sub>Cl in PBS for 10 min and washed in PBS.

VACV samples were imaged in STORM buffer on a Zeiss Elyra PS.1 system, using a 100× TIRF objective with additional 1.6× magnification (as above) for SIM, SRRF and SMLM acquisition (Supplementary Note 7). Buffer was exchanged to PBS and STED images were acquired on a Leica SP8, re-localizing the same region of interest based on the grid. SMLM data acquisition parameters were 30,000 frames at 100% laser power 647 nm illumination with 405 nm stimulation and an exposure time of 33 ms per frame.

**Clathrin coated pits sample preparation and imaging.** Rat glial cells (from embryonic day 18 pups) were cultured on 18-mm coverslips at a density of 4000 /cm<sup>2</sup>, respectively. After 9 days in culture, samples were fixed using 4% PFA in PEM (80 mM PIPES, 2 mM MgCl<sub>2</sub>, 5 mM EGTA, pH 6.8) for 10 min. For PAINT imaging<sup>23</sup> of clathrin coated pits (CCPs) in glial cells, fixed samples were incubated with a rabbit anti-clathrin primary antibody (abCam, catalog #21679) overnight at 4 °C, then with an anti-rabbit DNA-conjugated secondary antibody (Ultivue) for 1 h at room temperature.

DNA-PAINT imaging of CCPs in glial cells (Supplementary Note 10) was performed on a N-STORM microscope using a 100× objective as above. The same glial cell (present in low numbers in hippocampal cultures) was imaged in serial dilutions of Imager-650 (2 mM stock, from lower to higher concentration) in Imaging Buffer (Ultivue). The sample was illuminated at 647 nm (50% laser power) and a sequence of 20,000 images at



33 Hz was acquired for each Imager-650 dilution, before switching to a higher concentration of Imager-650 in Imaging Buffer.

**Actin rings sample preparation and imaging.** Rat hippocampal neurons (from embryonic day 18 pups) were cultured on 18-mm coverslips at a density of 10,000. After 9 days in culture, samples were fixed using 4% PFA in PEM (80 mM PIPES, 2 mM MgCl<sub>2</sub>, 5 mM EGTA, pH 6.8) for 10 min. Preparation of actin-stained neurons for SMLM was performed similarly to the protocol described in<sup>24</sup>, with minor modifications. After blocking, neurons were incubated with a mouse anti-map2 primary antibody (Sigma Aldrich, catalog #M4403) for 1h 30 min at room temperature (RT), then with a Alexa Fluor 488-labeled donkey anti-mouse secondary antibody (Thermo Fisher) for 45 min at RT, then with 0.5 mM phalloidin-Alexa Fluor 647 (Thermo Fisher) overnight at 4 °C. Neurons were mounted in a modified STORM buffer (50 mM Tris, pH 8, 10 mM NaCl, 10% glucose, 100 mM mercaptoethylamine, 3.5 U/ml pyranose oxidase, 40 µg/mL catalase) complemented with 0.05 mM phalloidin-Alexa Fluor 647, to mitigate phalloidin unbinding during acquisition and imaged immediately.

Neuron samples were imaged on a N-STORM microscope using a 100× objective as above (**Supplementary Note 11**). The sample was illuminated at 100% laser power at 647 nm. A sequence of 60,000 images at 67 Hz was acquired. Images were rendered with ThunderSTORM using a normalized 20 nm Gaussian from particle tables generated with SMAP, a MATLAB based software package developed by the Ries group at the EMBL, Heidelberg. Localizations were determined using a probability based method after background subtraction by wavelet filtering and lateral drift was corrected by cross-correlation.

**Visibility analysis.** To quantify the quality of the super-resolution reconstructions of parallel actin rings (**Supplementary Note 11**), a normalized visibility similar to that described in Geissbuehler *et al.*<sup>25</sup> was calculated as follows. Average intensity profiles were plotted for a 0.5 × 1 µm stretch of axon containing 5 actin rings for each of the 120 reconstructed images. The MATLAB function findpeaks was used to find the 5 peak positions in the average

profile measured from the 60,000 frames reconstruction, and mean pairwise visibility was calculated as follows.

$$\bar{v} = \frac{1}{2} \sum_{i=1}^4 \left( \frac{I_{\max,i} - I_{\min,i \rightarrow i+1} + I_{\max,i+1} - I_{\min,i \rightarrow i+1}}{I_{\max,i} + I_{\min,i \rightarrow i+1} + I_{\max,i+1} + I_{\min,i \rightarrow i+1}} \right)$$

$I_{\max,i}$  and  $I_{\max,i+1}$  are the intensities at peak positions  $i$  and  $i + 1$ , respectively, where  $i$  denotes the index of the actin ring in the sampled regions and  $I_{\min,i \rightarrow i+1}$  is the intensity at the midpoint of two adjacent peaks. Higher visibilities correspond to a greater ability to differentiate between two structures up to a maximum value of  $\bar{v}=0.5$ .

**Color maps.** Color maps used for displaying images ('NanoJ-Orange'), error maps ('SQUIRREL-errors') and FRC maps ('SQUIRREL-FRC') are provided in the NanoJ-SQUIRREL software package.

**Software availability.** The version of NanoJ-SQUIRREL used in this paper is available as **Supplementary Software**. The most recent version of NanoJ-SQUIRREL can be downloaded and installed in ImageJ and Fiji automatically by following the instructions in the manual, available here: <https://bitbucket.org/rhenriqueslab/nanoj-squirrel>. Source code is also available at the same website.

**Data availability.** The data that support the findings of this study are available from the corresponding authors upon reasonable request. Sample data sets can be downloaded from <https://bitbucket.org/rhenriqueslab/nanoj-squirrel>.

19. Müller, M., Mönkemöller, V., Hennig, S., Hübner, W. & Huser, T. *Nat. Commun.* **7**, 10980 (2016).
20. Kirshner, H., Aquet, F., Sage, D. & Unser, M. *J. Microsc.* **249**, 13–25 (2013).
21. Schmidt, F.I. *et al. Cell Rep.* **4**, 464–476 (2013).
22. Albrecht, D. *et al. J. Cell Biol.* **215**, 37 (2016).
23. Jungmann, R. *et al. Nat. Methods* **11**, 313–318 (2014).
24. Ganguly, A. *et al. J. Cell Biol.* **210**, 401–417 (2015).
25. Geissbuehler, S., Dellagiacomma, C. & Lasser, T. *Biomed. Opt. Express* **2**, 408–420 (2011).

## Life Sciences Reporting Summary

Nature Research wishes to improve the reproducibility of the work that we publish. This form is intended for publication with all accepted life science papers and provides structure for consistency and transparency in reporting. Every life science submission will use this form; some list items might not apply to an individual manuscript, but all fields must be completed for clarity.

For further information on the points included in this form, see [Reporting Life Sciences Research](#). For further information on Nature Research policies, including our [data availability policy](#), see [Authors & Referees](#) and the [Editorial Policy Checklist](#).

## ▶ Experimental design

## 1. Sample size

Describe how sample size was determined.

We aimed to acquire at least 5 data sets for each experimental data set and analysed these to validate repeatability of the algorithm. One representative data set was then chosen for display for each experiment. The number of repeats performed for simulations was determined by simulation run-time.

## 2. Data exclusions

Describe any data exclusions.

No data were excluded.

## 3. Replication

Describe whether the experimental findings were reliably reproduced.

Repeatedly running the same image through the SQUIRREL software yielded near-identical error maps and quality metrics each time.

## 4. Randomization

Describe how samples/organisms/participants were allocated into experimental groups.

Randomization was not relevant as our manuscript presents an analytical tool for image analysis.

## 5. Blinding

Describe whether the investigators were blinded to group allocation during data collection and/or analysis.

Blinding was not relevant as all data acquired for the experiments were analysed using the software described in this manuscript.

Note: all studies involving animals and/or human research participants must disclose whether blinding and randomization were used.

## 6. Statistical parameters

For all figures and tables that use statistical methods, confirm that the following items are present in relevant figure legends (or in the Methods section if additional space is needed).

n/a Confirmed

- The exact sample size ( $n$ ) for each experimental group/condition, given as a discrete number and unit of measurement (animals, litters, cultures, etc.)
- A description of how samples were collected, noting whether measurements were taken from distinct samples or whether the same sample was measured repeatedly
- A statement indicating how many times each experiment was replicated
- The statistical test(s) used and whether they are one- or two-sided (note: only common tests should be described solely by name; more complex techniques should be described in the Methods section)
- A description of any assumptions or corrections, such as an adjustment for multiple comparisons
- The test results (e.g.  $P$  values) given as exact values whenever possible and with confidence intervals noted
- A clear description of statistics including central tendency (e.g. median, mean) and variation (e.g. standard deviation, interquartile range)
- Clearly defined error bars

See the web collection on [statistics for biologists](#) for further resources and guidance.

## ► Software

Policy information about [availability of computer code](#)

### 7. Software

Describe the software used to analyze the data in this study.

Our study presents a novel software package for quantifying super-resolution image quality; the software itself is fully described in the manuscript and supplementary information and a link is provided for downloading the software. All image analysis was performed using Fiji (ImageJ 1.51n), and where published plugins have been used for image reconstruction (QuickPALM (v1.1), ThunderSTORM (version dev-2016-09-10-b1), SRRF (version 1.13Stable1) the settings have been described in the Methods section. The PSF Generator (v1.0.0), SIMcheck (v1.0.0) and fairSIM (v1.0.2) plugins were used in the supplementary information. The SuReSim software package (v0.5.1) was used for simulations in Figure 1.

For manuscripts utilizing custom algorithms or software that are central to the paper but not yet described in the published literature, software must be made available to editors and reviewers upon request. We strongly encourage code deposition in a community repository (e.g. GitHub). *Nature Methods* [guidance for providing algorithms and software for publication](#) provides further information on this topic.

## ► Materials and reagents

Policy information about [availability of materials](#)

### 8. Materials availability

Indicate whether there are restrictions on availability of unique materials or if these materials are only available for distribution by a for-profit company.

No unique materials were used

### 9. Antibodies

Describe the antibodies used and how they were validated for use in the system under study (i.e. assay and species).

Primary antibody for microtubule imaging in HeLa, CHO and COS cells: mouse monoclonal anti-alpha-tubulin, clone DM1A, Sigma catalog number T9026 (validation as per manufacturer's website: indirect immunofluorescence 1:500 using cultured chicken fibroblasts with cross-reactivity validated in human cell lines. Immunofluorescence images for hamster and human cell lines are available on the manufacturer's website). For COS cells an additional primary antibody was used: mouse monoclonal anti-alpha-tubulin, clone B-5-1-2, Sigma catalog number T5168 (validation as per manufacturer's website: indirect immunofluorescence 1:2000 using cultured human or chicken fibroblasts; cross-reactivity confirmed for African green monkey).  
Secondary antibody for microtubule imaging in HeLa, CHO and COS cells: goat anti-mouse IgG (H+L) highly cross-adsorbed Alexa Fluor 647, ThermoFisher Scientific catalog number A-21236.  
Primary antibody for clathrin-coated pit imaging in rat glial cells: rabbit polyclonal to clathrin heavy chain, Abcam catalog number Ab21679 (validation as per manufacturer's website: immunofluorescence at concentration of 1µg/ml; reacts with rat)  
Secondary antibody for clathrin-coated pit imaging in rat glial cells: anti-rabbit DNA-conjugated, part of Ultivue kit Ultivue-2  
Anti-GFP nanobody for VACV lateral body imaging: GFP-Trap uncoupled protein, catalog number gt-250, Chromotek

### 10. Eukaryotic cell lines

a. State the source of each eukaryotic cell line used.

HeLa cells were kindly provided by Prof Mark Marsh, UCL  
CHO cells were originally provided by Ira Mellman, Genentech  
COS cells were obtained from ATCC.

b. Describe the method of cell line authentication used.

Cell lines were not authenticated

c. Report whether the cell lines were tested for mycoplasma contamination.

Cell lines tested negative for mycoplasma

d. If any of the cell lines used are listed in the database of commonly misidentified cell lines maintained by [ICLAC](#), provide a scientific rationale for their use.

No commonly misidentified cell lines were used.

## ► Animals and human research participants

Policy information about [studies involving animals](#); when reporting animal research, follow the [ARRIVE guidelines](#)

### 11. Description of research animals

Provide details on animals and/or animal-derived materials used in the study.

Wistar Rat hippocampal neurons and glial cells were harvested from embryonic day 18 pups, following established guidelines of the European Animal Care and Use Committee (86/609/CEE) and approval from the local ethics committee (agreement D13-055-8).

Policy information about [studies involving human research participants](#)

### 12. Description of human research participants

Describe the covariate-relevant population characteristics of the human research participants.

This study did not involve human research participants.